On-Body Path Loss Modeling in the 110 GHz to 170 GHz Frequency Range

Brecht De Beelde, Arno Thielens, Reza Aminzadeh, and Wout Joseph

Abstract – This article presents empirical on-body path loss (PL) models for RF electromagnetic fields at frequencies in the *D* band. For the first time, PL is measured at frequencies from 110 GHz to 170 GHz, with the antennas placed at heights of 1 mm to 6 mm above a skin phantom, and with very small antenna separations from 1 cm to 19 cm. PL is measured using a vector network analyzer-based channel sounder with frequency extenders and using vertically and horizontally polarized horn antennas. The measured PL is fitted to an alpha–beta–gamma model, and wideband PL is fitted to a floating intercept model. Both models have a high reference PL and low PL exponent below one. Even though the frequency dependence is small, PL increases with frequency. The measured PL is higher when the antennas are closer to the skin phantom.

1. Introduction

In the last decade, the domain of personal area networks has evolved into wireless body area networks (WBANs), where sensor and actuator nodes in and on the body wirelessly transmit data to each other [1] or off the body [2]. Numerous channel models for WBANs at frequencies below 10 GHz are available [3], and WBANs operational at millimeter-wave frequencies are being deployed (e.g., in the *V* band at 60 GHz [4–6] and the *W* band around 94 GHz [7, 8]).

On-body path loss (PL) is generally studied using three approaches: theoretical [4, 5], numerical [9], and using measurements [4, 6, 9]. On-body measurements have the disadvantages that they introduce subject-to-subject variation [10] and that it is difficult for a subject to remain immobile. Therefore, human body-mimicking objects, so-called *phantoms*, are used to stabilize and standardize these measurements [4].

It is envisioned that future communication systems, including sixth-generation wireless networks, will be important for the realization of WBANs [11], for example, in applications such as wireless prosthetics, when large data rates are required over separation distances below 20 cm [10]. These future communication systems may use frequencies above 100 GHz, such as the *D* band, with frequencies ranging from 110 GHz to 170 GHz. The *D*-band channel models are available for indoor [12, 13] and outdoor [14, 15] environments. In this article, we present an on-body PL model for *D*-band frequencies. For the first time, on-phantom PL measurements are performed above 100 GHz to characterize the radio channel for short-range high-data rate wireless communication in WBANs. Compared with the existing *D*-band channel models, not only is the presence of the skin near the line-of-sight (LOS) path important, but also the antenna separation is limited as well.

Manuscript received 27 December 2022. This work was performed within the IMEC D-Band Channel Modeling research project. Arno Thielens is a postdoctoral fellow of the Research Foundation–Flanders (grant agreement 1283921N).

Brecht De Beelde, Arno Thielens, and Wout Joseph are with the Department of Information Technology, Ghent University, IMEC, Technologiepark-Zwijnaarde 126, 9052, Ghent, Belgium; e-mail: Brecht.DeBeelde@gmail.com; Arno.Thielens@UGent.be; Wout.Joseph@UGent.be.

Reza Aminzadeh is with Unitron Group, Frankrijklaan 27, 8970, Poperinge, Belgium; e-mail: Reza.Aminzadeh@unitrongroup.com.

2. Methodology

A vector network analyzer (VNA) with frequency extenders is used to perform *D*-band channel measurements for antenna separations up to 19 cm, with a skin phantom positioned between the antennas. In the remainder of this article, we will refer to on-body PL measurements when the skin phantom is present near the antennas. This measurement setup is presented in Figure 1.

2.1 Channel Sounder

The VNA-based channel sounder that is presented and validated in [16] is used for the channel measurements. QuinStar standard gain pyramidal horn antennas (type QWH-DPRR00) are connected to the rectangular waveguides (WR-6) of the frequency extenders. The antennas are operational in the *D* band and have a gain increasing from 22.2 dBi for 110 GHz to 23.3 dBi for 170 GHz. The antennas have an *H*-plane half-power beamwidth (HPBW), ranging from 13.2° at 110 GHz to 12° at 170 GHz, and an *E*-plane HPBW ranging from 12° at 110 GHz to 8.8° at 170 GHz. The Fraunhofer far-field distance d_F of these antennas, calculated via

$$d_F = \frac{2D^2}{\lambda} \tag{1}$$

equals 0.55 m at 170 GHz, as D is equal to 0.022 m, and the wavelength λ is 0.00176 m.

A frequency sweep is performed with 3001 frequency points and a frequency step size of 20 MHz. The IF measurement bandwidth of the VNA is set to 100 Hz. The output power is set to 16 dBm. A normalized forward calibration is performed before all measurements, with the frequency extender waveguides as the reference plane of the calibration. No averaging is

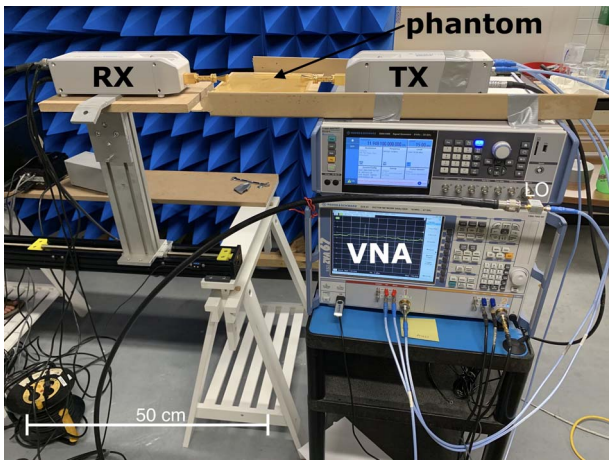

Figure 1. The measurement setup with a VNA-based channel sounder.

performed on the VNA, but each measurement is performed three times. The VNA sweep time is 45 s during which the channel is assumed to be static, as no people were moving during the measurements.

The IF bandwidth and transmit power settings result in a dynamic range of the sounder of 95 dB. Due to the high bandwidth, a high temporal resolution $\Delta\tau$ of 0.0167 ns is obtained. The maximum resolvable time delay of 50 ns corresponds to a path length of 15 m.

2.2 Measurement Scenarios

Before the on-body measurements, reference measurements were performed and used to evaluate antenna gains, cable losses, and conversion losses over the full band [16]. The antenna separation during the reference measurements was 1.5 m (i.e., the antennas are in the far field), and no obstacles were present in between the antennas.

For the on-body PL measurements, the antenna separation ranged from 1 cm to 19 cm, by moving the receive (RX) antenna away from the transmit (TX) antenna in steps of 3 cm. A skin phantom was placed between the antennas. The antennas were placed at different heights above the skin phantom of 1 mm, 3 mm, and 6 mm, respectively. Measurements were performed with both horizontal (HH) and vertical (VV) copolarized antennas, by rotating the convertors by 90°.

2.3 Skin Phantom

A low-cost tissue-equivalent phantom measuring 20 cm by 15 cm was used to emulate the dielectric properties of a human skin. It has a thickness of 15 mm and is composed of 69.3% deionized water, 29.7% gelatin powder, and ~1% agar–agar [17]. This phantom was characterized for frequencies up to 40 GHz, but it is considered to be representative for *D*-band frequencies based on the following observations: i) in [18], a similar phantom with only 1.4% increased mass of gelatin powder was shown to represent the skin's dielectric properties up to 100 GHz; ii) in [19], an analytical model of the human skin with a water content of 70% was validated with measurement data from literature <100 GHz, and a maximum deviation of 10% was reported. In addition, it was shown that this deviation decreased for increasing frequencies. Hence, we assume that this downward trend in error would continue in the *D* band.

2.4 Data Processing

From the measured transfer function $H(f)$, PL (in decibels) is obtained via

$$\mathrm{PL}(f) = -10\log_{10}\left(\frac{1}{N}\sum_{i=1}^{N}|H_i(f)|^2\right) + 2G_a(f) + C(f) \tag{2}$$

with N the number of frequency sweeps, $G_a(f)$ the frequency-dependent antenna gain, and $C(f)$ a correction term based on the reference measurements [16]. After applying the Hann window $\mathcal{W}$, the inverse discrete Fourier transformation of the transfer function $H(f)$ results in the channel impulse response from which the averaged power delay profile (PDP) is found. This is mathematically formulated as

$$\mathrm{PDP}(k\Delta\tau) = \frac{1}{N}\sum_{i=1}^{N}|\mathrm{IDFT}(\mathcal{W}(f)\cdot H_i(f))|^2 \tag{3}$$

From the PDP, wideband on-body PL is obtained. First, the power of the first peak of the PDP of the reference measurements (with an antenna separation of 1.5 m) is compared with free-space PL (FSPL), calculated via

$$\mathrm{FSPL}(d,f) = 20\log_{10}\left(4\pi d\frac{f}{c}\right) \tag{4}$$

with d the distance in meters, f the frequency in hertz, and c the speed of light. The offset (caused by antenna gains and cable losses) is then added to the power of the first peak of the PDP of the on-body PL measurements. This is represented via

$$\mathrm{PL} = -\max(\mathrm{PDP}) + (\mathrm{FSPL}(1.5\,\mathrm{m}, 140\cdot 10^9\mathrm{Hz}) + \max(\mathrm{PDP}_{\mathrm{ref},\,1.5\,\mathrm{m}})) \tag{5}$$

in which the first term is the peak of the PDP of the on-body measurements (positive value) and the second term is the offset between the peak the PDP of the reference measurements and FSPL.

2.5 PL Models

Measured PL as a function of frequency, obtained via (2), is fitted to the alpha–beta–gamma (ABG) model

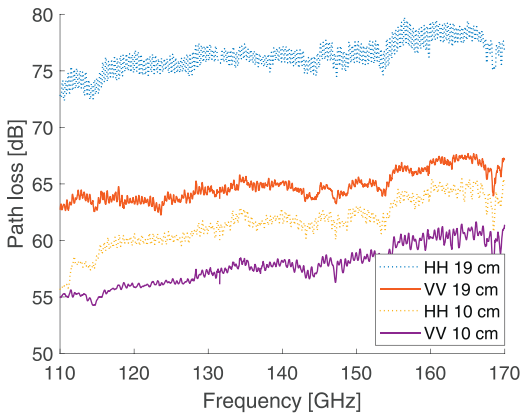

Figure 2. Measured PL as a function of frequency for an antenna height of 1 mm above the skin phantom, antenna separations 10 cm and 19 cm, and VV and HH copolarizations.

$$\mathrm{PL}_{\mathrm{ABG}}(d,f) = \alpha + 10\beta\log_{10}\left(\frac{d}{d_0}\right) + 10\gamma\log_{10}\left(\frac{f}{f_0}\right) + \chi_\sigma \tag{6}$$

with d the distance in meters, d_0 the reference distance, f the frequency in gigahertz, and f_0 the reference frequency. In this work, a reference distance d_0 of 1 cm and a reference frequency f_0 of 1 GHz are selected. The model parameter α is the floating intercept in decibels (i.e., the PL for distance d_0 at frequency f_0, β is the dimensionless PL exponent, γ is the dependence of PL on frequency, and χ_σ is the shadow fading term in decibels [20]).

Wideband PL, obtained via (5), is fitted to the floating intercept (FI) PL model

$$\mathrm{PL}_{\mathrm{FI}}(d) = \mathrm{PL}_0 + 10n\log_{10}(d/d_0) + \chi_\sigma \tag{7}$$

with d the distance in meters, d_0 the reference distance of 1 cm, and PL exponent n. The shadow fading term χ_σ in decibels is again based on a zero-mean normal distribution with standard deviation σ.

3. Results and Discussion

3.1 Frequency-Dependent PL

Figure 2 visualizes measured PL as a function of frequency for two polarizations and two distances, with an antenna height of 1 mm. Fitting the measurement data to the ABG model from (6) results in the fitted parameters listed in Table 1. Both the PL exponent β and frequency dependence γ are smaller than the free-space value of two. The P values of all fitted parameters are below the significance level of 10^{-3}. The error between the model and measured PL samples across all frequency and distance samples follows a normal distribution with zero mean and a standard variation close to the root-mean-square error (RMSE).

Table 1. Fitted parameters of the ABG model for different polarizations (P) and antenna heights (H) above the skin phantom

P	H (mm)	α (dB)	β	γ	RMSE (dB)
VV	1	44.6	0.54	0.48	2.7
VV	3	38.0	0.81	0.62	3.3
VV	6	41.2	0.65	0.54	2.6
HH	1	26.6	3.13	0.30	3.0
HH	3	44.5	0.68	0.36	2.3
HH	6	45.5	0.60	0.34	2.2

The measured PL is higher than FSPL, and the highest PL is measured for the lowest height of 1 mm above the skin phantom. Moreover, the measured PL is higher for HH copolarized antennas than for VV copolarized antennas. The values for β and γ are low compared with the higher PL exponents ranging from two to five that are reported at millimeter-wave frequencies [5, 6]. This is explained by the small antenna separations that near-field effects need to be considered, whereas the PL calculation in (2) considers the far-field antenna gain. A larger antenna inefficiency at small antenna separations results in the high measured PL values for smaller distances, which results in a smaller slope (i.e., a high reference PL for α and low fitted values for β and γ).

3.2 Wideband PL

Figure 3 shows the PDP for some select measurement scenarios. It is clear that round-trip reflections (i.e., reflections on the TX and RX antennas) are present. The reflections on the skin phantom cannot be resolved, as the direct and reflected path lengths differ by less than 5 mm.

Wideband PL is obtained by selecting the power of the first peak and converting it into PL via (5). The measured PL as a function of distance is shown in Figure 4. From this figure, the high PL for small distances is clear, which results in the low PL exponent β from Table 1. When fitting all PL samples to the FI model from (7), similar PL exponents are obtained.

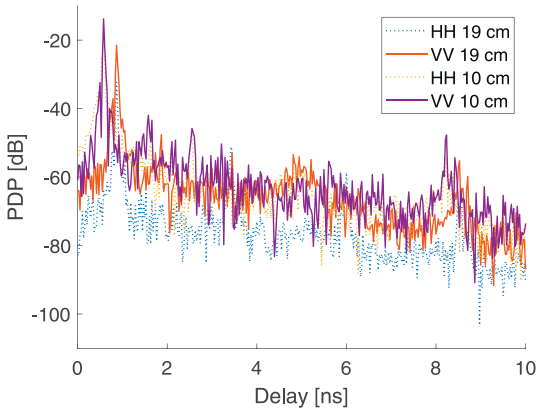

Figure 3. The PDP for different antenna separations and polarizations, with the antennas placed at 1 mm above the skin phantom.

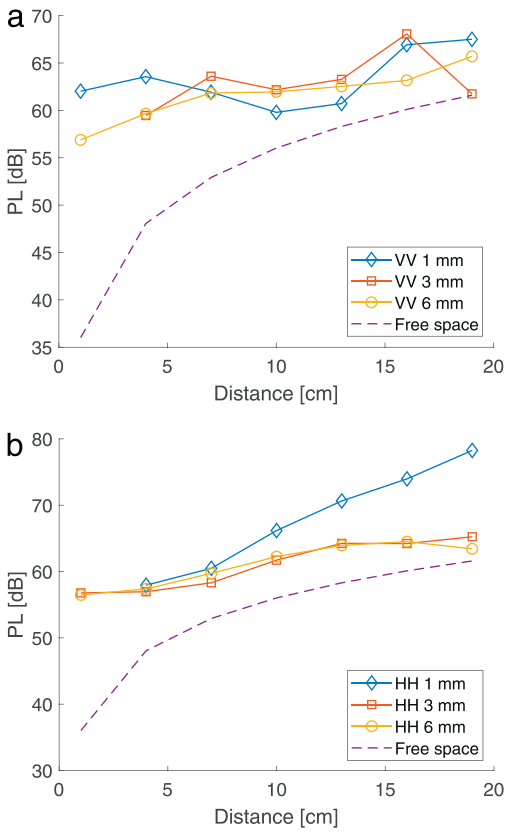

Figure 4. Measured wideband PL as a function of distance for different antenna heights. (a) VV, (b) HH.

Table 2 lists the fitted parameters of the FI PL model when only antenna separations ranging from 10 cm to 19 cm are considered.

The difference between measured PL and FSPL is higher for small distances, due to a bad performance of the antennas (i.e., they are too close for efficient radiation). Due to the high PL for small distances, both the ABG and FI models result in a PL exponent well below two, with a reference PL above FSPL. PL is lower when the antennas are placed at a higher height above the skin phantom.

4. Conclusions

In this article, an on-body measurement campaign is presented at *D*-band frequencies, ranging from 110 GHz to 170 GHz. The influence of distance, frequency, antenna height above the skin phantom, and polarization are investigated. With an increased frequency, and using waveguide-based antennas, the far-field distance of the antennas increases. At small antenna separations, the antennas do not efficiently radiate, and the boundary conditions on the phantom cause adverse propagation conditions, resulting in a high measured PL. Furthermore, when the antennas are placed above the skin, the boundary conditions are unfavorable for *H* polarization due to current cancelation, and the mirror effect can cause interference in *V* polarization. Both effects result in a PL model with a high reference PL and low PL exponent. The PL is higher when the height above the phantom is lower and for a horizontally copolarized antenna setup. The latter can be caused by the larger HPBW of the antennas in the *H* plane. The PL exponent is similar to values reported in literature when only antenna separations above 10 cm are considered. Future work includes analyzing the impact of different shapes of the phantom, while considering LOS path blockage and antenna mismatch (e.g., caused by a wrist rotation), and a full characterization of the skin phantom at *D*-band frequencies. Furthermore, the comparison of the measurements with numerical simulations and the validation of the PL models on a real human body is pending. Moreover, a joint antenna and channel model in which the antenna and channel characteristics are jointly evaluated would be beneficial.

Table 2. Fitted parameters of the FI model for different polarizations (P) and antenna heights (H) above the skin phantom for distances from 10 cm to 19 cm

P	H (mm)	PL_0 (dB)	n	RMSE (dB)
VV	1	27.7	3.14	1.8
VV	3	56.6	0.65	2.6
VV	6	49.2	1.23	0.9
HH	1	23.5	4.24	0.6
HH	3	50.5	1.17	0.7
HH	6	55.3	0.67	1.4

5. References

1. M. Patel and J. Wang, "Applications, Challenges, and Prospective in Emerging Body Area Networking Technologies," *IEEE Wireless Communications*, **17**, 1, February 2010, pp. 80-88.
2. M. Marinova, A. Thielens, E. Tanghe, L. Vallozzi, G. Vermeeren, et al., "Diversity Performance of Off-Body MB-OFDM UWB-MIMO," *IEEE Transactions on Antennas and Propagation*, **63**, 7, July 2015, pp. 3187-3197.
3. S. van Roy, C. Oestges, F. Horlin, and P. De Doncker, "A Comprehensive Channel Model for UWB Multisensor Multiantenna Body Area Networks," *IEEE Transactions on Antennas and Propagation*, **58**, 1, January 2010, pp. 163-170.
4. N. Chahat, G. Valerio, M. Zhadobov, and R. Sauleau, "On-Body Propagation at 60 GHz," *IEEE Transactions on Antennas and Propagation*, **61**, 4, April 2013, pp. 1876-1888.
5. L. Petrillo, T. Mavridis, J. Sarrazin, D. Lautru, A. Benlarbi-Delaï, et al., "Analytical Creeping Wave Model and Measurements for 60 GHz Body Area Networks," *IEEE Transactions on Antennas and Propagation*, **62**, 8, August 2014, pp. 4352-4356.
6. R. Aminzadeh, A. Thielens, M. Zhadobov, L. Martens, and W. Joseph, "WBAN Channel Modeling for 900 MHz and 60 GHz Communications," *IEEE Transactions on Antennas and Propagation*, **69**, 7, July 2021, pp. 4083-4092.
7. A. Brizzi, A. Pellegrini, L. Zhang, and Y. Hao, "Statistical Path-Loss Model for On-Body Communications at 94 GHz," *IEEE Transactions on Antennas and Propagation*, **61**, 11, November 2013, pp. 5744-5753.
8. K. Ali, A. Brizzi, A. N. Khan, and Y. Hao, "On-Body NLOS Radio Channel at Millimeter Wave Frequencies,"

IEEE Transactions on Antennas and Propagation, **72**, 2, February 2023, pp. 1783-1792.

9. E. Reusens, W. Joseph, B. Latré, B. Braem, G. Vermeeren, et al., "Characterization of On-Body Communication Channel and Energy Efficient Topology Design for Wireless Body Area Networks," *IEEE Transactions on Information Technology in Biomedicine*, **13**, 6, November 2009, pp. 933-945.
10. R. Proesmans, K. Deprez, M. Velghe, and A. Thielens, "An On-Body Antenna for Control of a Wireless Prosthesis in the 2.45 GHz Industrial Scientific and Medical Frequency Band," *IET Microwaves, Antennas & Propagation*, **16**, 15, December 2022, pp. 919-932.
11. B. Cornet, H. Fang, H. Ngo, E. W. Boyer, and H. Wang, "An Overview of Wireless Body Area Networks for Mobile Health Applications," *IEEE Network*, **36**, 1, February 2022, pp. 76-82.
12. B. De Beelde, D. Plets, C. Desset, E. Tanghe, A. Bourdoux, et al., "Material Characterization and Radio Channel Modeling at D-Band Frequencies," *IEEE Access*, **9**, November 2021, pp. 153528-153539.
13. L. Pometcu and R. D'Errico, "An Indoor Channel Model for High Data-Rate Communications in D-Band," *IEEE Access*, **8**, December 2020, pp. 9420-9433.
14. B. De Beelde, R. De Beelde, E. Tanghe, D. Plets, K. Verheyen, et al., "Vegetation Loss at D-Band Frequencies and New Vegetation-Dependent Exponential Decay Model," *IEEE Transactions on Antennas and Propagation*, **70**, 12, December 2022, pp. 12092-12103.
15. B. De Beelde, E. Tanghe, D. Plets, and W. Joseph, "Outdoor Channel Modeling at D-Band Frequencies for Future Fixed Wireless Access Applications," *IEEE Wireless Communications Letters*, **11**, 11, November 2022, pp. 2355-2359.
16. B. De Beelde, D. Plets, E. Tanghe, and W. Joseph, "Directional Sub-THz Antenna-Channel Modelling for Indoor Scenarios," 2021 15th European Conference on Antennas and Propagation, Dusseldorf, Germany, March 22–26, 2021.
17. R. Aminzadeh, M. Saviz, and A. Shishegar, "Theoretical and Experimental Broadband Tissue-Equivalent Phantoms at Microwave and Millimetre-Wave Frequencies," *Electronics Letters*, **50**, 8, April 2014, pp. 618-620.
18. R. Aminzadeh, M. Saviz, and A. A. Shishegar, "Comments on "Wideband Skin-Equivalent Phantom for V- and W-band," *IEEE Antennas and Wireless Propagation Letters*, **16**, March 2017, pp. 3257-3257.
19. R. Aminzadeh, *Simulation and Assessment of Millimeter-Wave Reflectometry for Detection of Skin Cancers*, Master's thesis, Sharif University of Technology, Tehran, Iran, 2014.
20. S. Salous, J. Lee, M. D. Kim, M. Sasaki, W. Yamada, et al., "Radio Propagation Measurements and Modeling for Standardization of the Site General Path Loss Model in International Telecommunications Union Recommendations for 5G Wireless Networks," *Radio Science*, **55**, 1, January 2020, p. e2019RS006924.